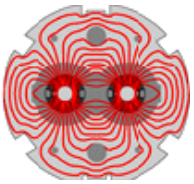

LHC Project Note 402

Simone.Gilardoni@cern.ch,
John.Jowett@cern.ch

2007-01-30

Beam Loss Monitors for Heavy Ion Operation

G. Bellodi, H.H. Braun, R. Bruce, S. Gilardoni, J.M. Jowett /AB-ABP

Keywords: heavy-ion, beam-loss, collimation, LHC

Summary

The performance of the LHC as a heavy-ion collider is expected to be limited by a variety of beam loss mechanisms that are non-existent, or substantially different, in the case of protons. Among these are ultra-peripheral interactions of the colliding beams and the collimation inefficiency. Loss patterns are different and require additional installations of beam loss monitors. Further, the relation between energy deposition in superconducting magnet coils and the loss monitor signals has to be reassessed for heavy ions in order to determine the thresholds for dumping beams.

1. Introduction

In order to monitor particle losses in the LHC and dump the beam if there is a risk of quenching the superconducting magnets, a beam loss monitor (BLM) system will be installed around the ring [1]. This system consists of ionization chambers that will detect secondary shower particles outside the magnet cryostat. The location of the BLMs and the loss thresholds for dumping the beam are primarily optimized for protons. The system will however also be used during heavy-ion runs, starting with $^{208}Pb^{82+}$ beams.

This note has three main parts: Section 2 treats the general problem of defining whether the type of BLMs and their thresholds for dumping the beam are also suitable for ions. We approach this by simulating the ratio between heat deposition in the superconducting coils of a magnet and the signal in the BLM system for both particle species, assuming a generic beam loss.

In the following two sections we deal with the more specific cases of protection against losses induced by collimation inefficiencies and secondary beams created by electromagnetic interactions at the interaction points (IPs). These losses are peculiar to heavy ion operation and we need to determine if the foreseen proton BLM coverage is sufficient.

2. Beam dump thresholds

2.1. Simulation setup

To compare the BLM signal beam-dump thresholds for Pb^{82+} and proton beams, the Monte Carlo code FLUKA [2,3] was used to simulate the development of showers generated by particle losses in a magnet. Simulations were done with both particle species in order to compare the ratio of heat deposited in the superconducting coil and the signal on the BLMs. The detailed geometry of a main dipole magnet (MB) was implemented in FLUKA and the BLMs were schematically modelled as thin rectangular iron boxes filled with nitrogen, placed outside the MB cryostat. This simplification is consistent with the simulations performed in [1] and can be considered fair since we are interested in the relationship between heat deposition from heavy ions and proton losses and not the absolute signal from the BLM. The geometry of the FLUKA model of the magnet is shown in Figure 1.

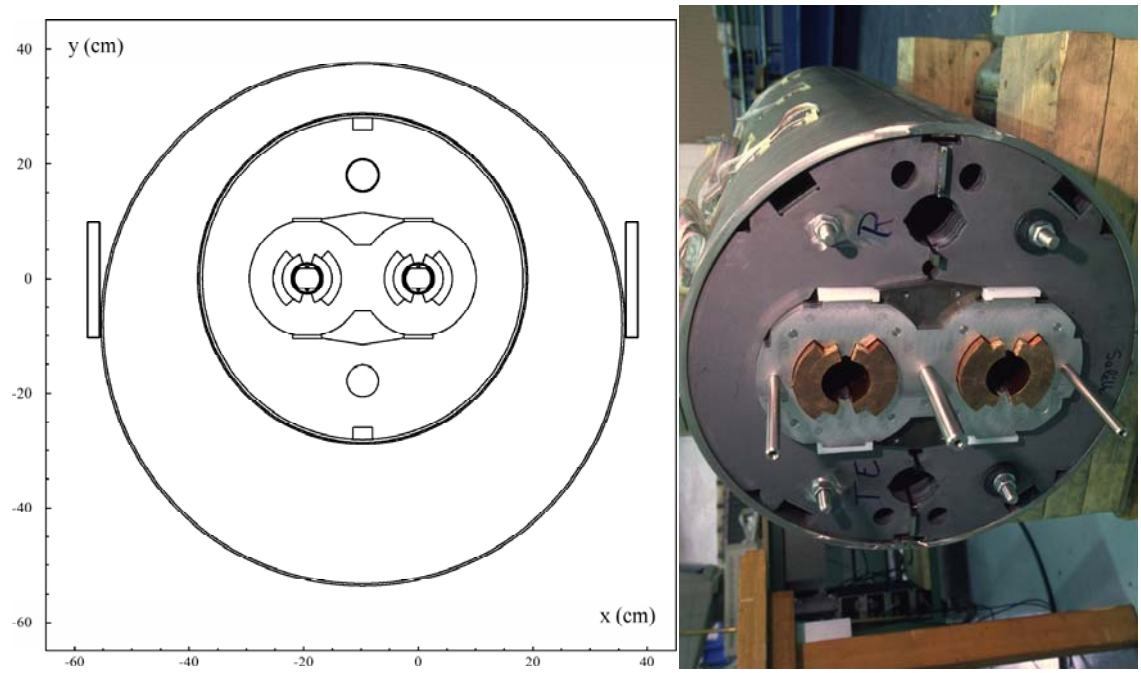

Figure 1 The transverse cross section of the FLUKA model of the dipole with the BLMs outside (left) compared with the section of a real dipole (right).

A generic beam loss was represented by a pencil beam of nominal LHC collision energy impinging on the inside of the vacuum chamber in negative x in the horizontal plane at a typical incident angle of 0.25 mrad and the shower was simulated in FLUKA. During the simulation, the energy deposition in the beam screen, in the superconducting coils and in the BLMs was scored. Since the BLM signal is proportional to the ionization energy loss in its gas volume and ionization is the dominant loss process for the low energy secondaries that escape outside the cryostat, this is a fair approximation. Simulations were done with both 7 TeV protons and 2.76A TeV lead ions.

2.2. Results

The resulting longitudinal energy deposition profiles in the hottest superconducting wire in the MB coil and in the BLMs are shown in Figure 2. In the wire, the energy deposition was averaged over a volume of approximately 2 cm^3 (5 cm longitudinal binning, transversal area corresponding approximately to the wire cross section). In order to facilitate the comparison,

the curves for the Pb^{82+} ions have been scaled with energy and number of nucleons. This is equivalent to scaling with charge, since the magnetic rigidity has to be the same for the two particles species in the same magnetic field. As can be seen in the figure, the two particle types have almost identical profiles. This means that the ratio between the heat deposited in the coils and the energy deposition in the BLMs is about the same for ions and protons and that, accordingly, the same beam dump thresholds can be used. The values of the thresholds are already decided for protons, and these simulations show that they do not need to be changed for the heavy ion runs.

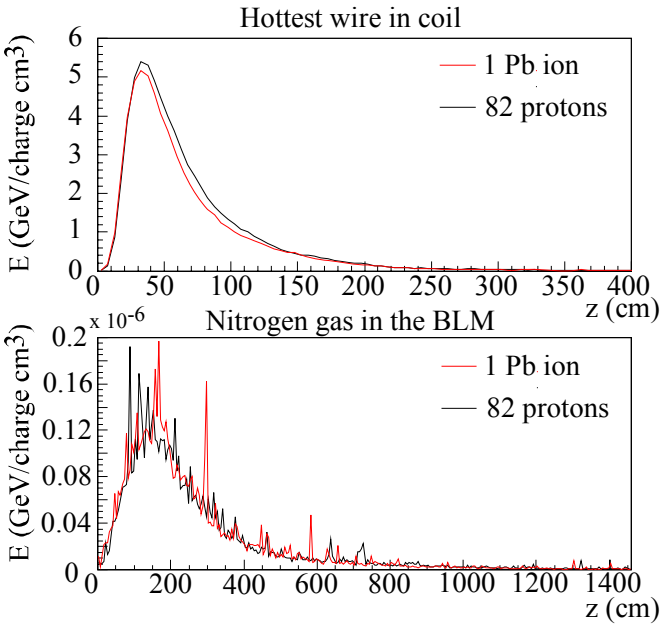

Figure 2. The energy deposition in the hottest wire in the coil and in the N_2 gas inside the BLM for Pb ions and protons.

At first sight, it may appear counter-intuitive that heavy ions and protons have similar shower profiles. We shall now try to explain why this is so.

2.3. Physics discussion

To understand the simulation result, the underlying physics processes must be analyzed. In this section we shall give a short description of the physics and demonstrate the plausibility of the simulation result.

When a charged particle enters a material it loses energy through interactions with the atomic electrons and nuclei of the target. The interaction with the electrons is purely electromagnetic while that with the nuclei proceeds via both electromagnetic and nuclear forces. At lower energies, the most important electromagnetic process for energy loss is ionization. Here atomic electrons are excited or set free from their corresponding nuclei through the Coulomb field of the impinging particle. The energy loss per unit path length through ionization is well described by the Bethe-Bloch formula [4]:

$$-\frac{dE}{dx} = 4\pi N_A r_e^2 m_e c^2 \frac{z^2 Z}{A\beta^2}\left(\frac{1}{2}\ln\left(\frac{2m_e c^2\beta^2\gamma^2 T_{\max}}{I^2}\right) - \beta^2 - \frac{\delta}{2}\right)$$

where βc is the speed of the particle, ze its charge, m_e the electron mass, Z and A the charge and mass number of the target, I its average excitation potential, N_A Avogadro's number, r_e the classical electron radius and δ a correction factor for the density effect at high energy. The energy loss of a $^{208}Pb^{82+}$ ion as a function of its energy per nucleon from this formula is shown in Figure 3.

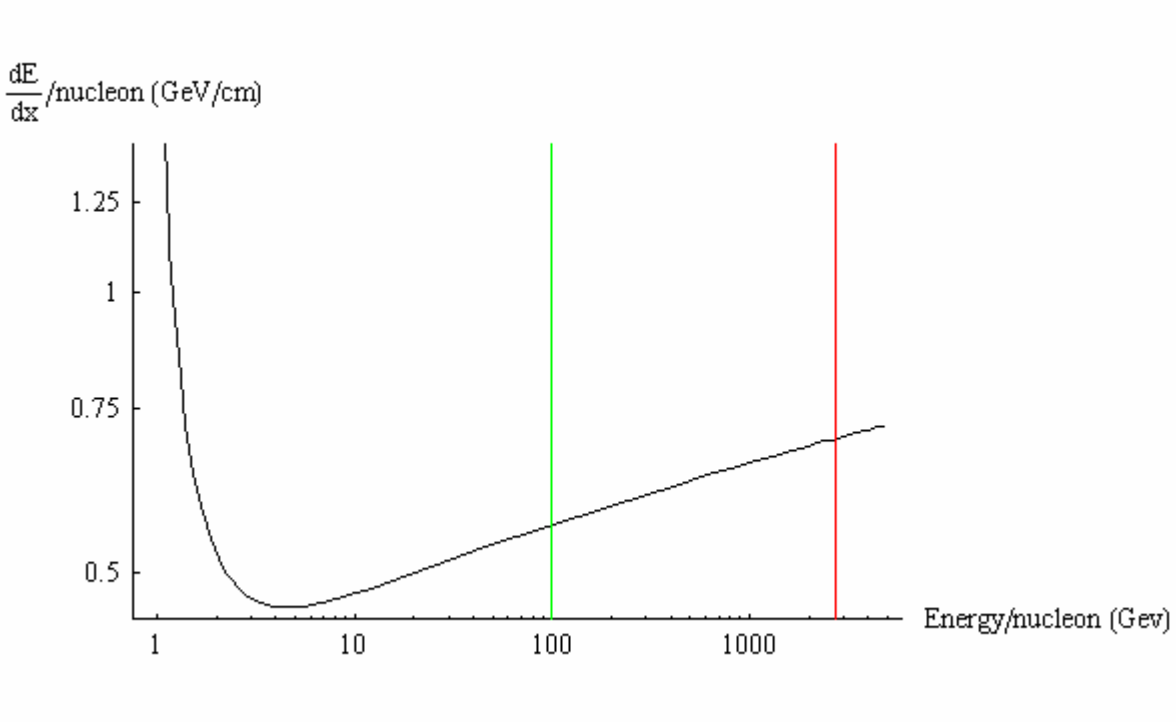

Figure 3 Energy deposition per unit path length for a $^{208}Pb^{82+}$ ion hitting a copper block as a function of energy. The LHC energy is marked in red. Inclusion of further correction terms make the curve approximately constant for ion energies above 100 A GeV (indicated in green) .

From the Bethe-Bloch formula it is clear that the deposited energy is proportional to the square of the charge of the impinging particle, so a $^{208}Pb^{82+}$ ion will deposit 82^2 times more energy through ionization than a proton with the same energy. On the other hand, the energy dependence is weak at high energies. For heavy ions there are also extra corrections, due to the finite nuclear size, that need to be taken into account [5,6], which make the energy deposition as a function of energy even flatter at high energy. In a crude approximation the deposited energy per unit path length for heavy ions is constant above 100 A GeV due to these extra corrections. This is indicated in green in Figure 3.

It is also worth noting that the ionization is a quite local process. The cross section is very high and a large number of interactions take place, but the electrons that are set free are mostly at low energy, so-called soft electrons. According to the shape of the Bethe-Bloch curve these electrons will lose their energy very quickly and stop close to their initial position, meaning that the main part of the ionization energy will be deposited very close to the trajectory of the impinging particle. Also some electrons with higher energy, the so-called δ-rays, are created, and they will travel further. However their contribution is smaller since the cross section for creating them is much smaller.

Electron-positron pair production is another mechanism for energy loss in the material, which becomes more important the higher the energy and the charge becomes. Both slow pairs, which deposit their energy after only a short distance, and fast pairs are created. Preliminary estimates with a new beta version of FLUKA have shown that pair production can increase the electromagnetic energy loss on the order of 40% for a $^{208}Pb^{82+}$ ion at LHC energy hitting a copper target. This is however ongoing work that will be published elsewhere [6].

Other electromagnetic processes include bremsstrahlung and photo nuclear reactions. Bremsstrahlung is very important for light particles, but is only a minor contribution even at ultra-relativistic energies for both heavy ions and protons. Bremsstrahlung and pair production together give rise to the electromagnetic shower, where the created photons convert into electron-positron pairs, which in turn radiate more bremsstrahlung. These processes as direct

energy deposition mechanisms from the primary particle are however much less important than the ionization for particles with a high z, so the difference in the electromagnetic energy deposition between the species is totally dominated by the high ionization and pair production cross section for the ions.

The energy deposition resulting from nuclear interactions on the other hand is similar for heavy ions and protons, even though the nuclear cross sections are very different (scaling approximately as $A^{2/3}$). Since the nuclear interaction length for ions is shorter, the first interaction will take place after a shorter distance than for protons. When the ion traverses the target material, the nucleus will also split up into smaller fragments through electromagnetic dissociation and nuclear interactions in several steps. After it is totally fragmented it will give rise to the same cross sections and shower profile as independent nucleons.

When the incoming particles interact inelastically with the target nuclei a wide spectrum of secondary particles is created. These particles in turn make new interactions—some of them, mainly π^0 mesons, will decay through electromagnetic interactions and thus also cause an electromagnetic shower. So after every interaction a larger and larger fraction of the total energy will be carried by the electromagnetic particles and the final energy deposition is often dominated by the electromagnetic part. At the shower maximum, a huge number of low energy particles are simultaneously depositing energy that in total by far exceeds the direct energy deposition from the first few interactions. This peak for ions is very similar to the one created by independent nucleons. In fact the hadronic shower from an ion can with good accuracy be modelled as the superposition of independent nucleons. This is often used in cosmic ray physics (see for instance [20,21]. No simple analytical approximations of the hadronic shower exist, so the energy deposition and the shower shape are instead often computed through Monte Carlo simulations.

In order to quantify the effect of direct ionization further FLUKA simulations were performed. They show that the heaviest remaining fragment of a 2.76 A TeV $^{208}Pb^{82+}$ ion entering a solid copper target on average has only 20% of the mass of the initial ion after 10 cm, and after 29 cm the ion is totally fragmented. The average mass of the heaviest surviving fragment from the FLUKA simulation is shown in Figure 4. As a cross check of the data analysis the cross sections were also estimated. From the simulations the cross section is found to be 5.1 barns for nuclear interactions and 12.2 barns for electromagnetic dissociation, which is consistent with the model that FLUKA is built on [7].

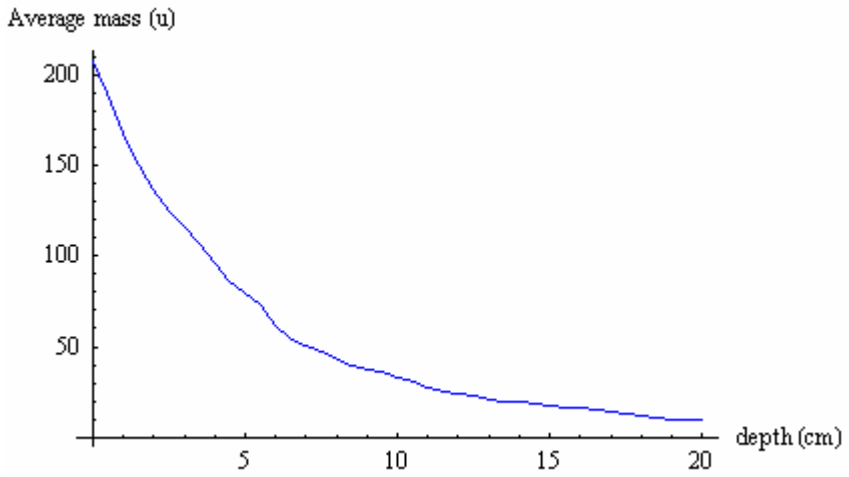

Figure 4. The average mass of the heaviest fragment of an impinging 2.76 A TeV Pb ion in a copper target as a function of penetration depth.

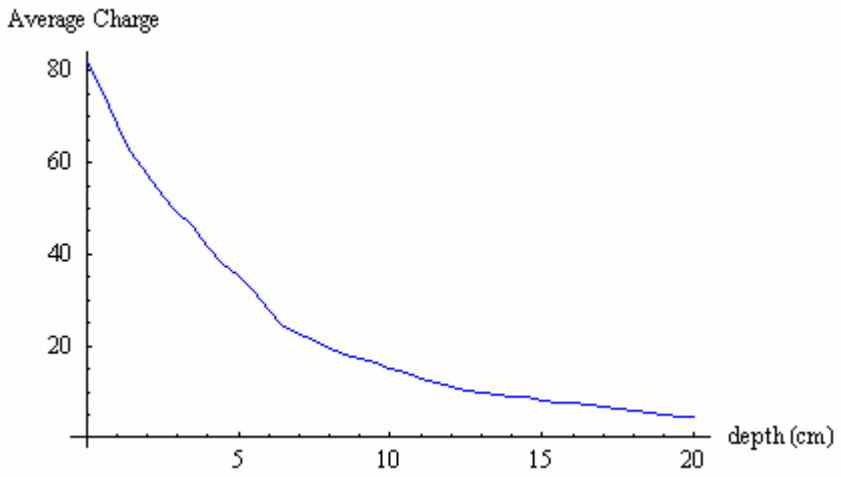

Figure 5. The average charge of the heaviest fragment of an impinging 2.76 A TeV Pb ion in a copper target as a function of penetration depth.

It is worth noting that the average mass of the heaviest fragment as a function of depth s in the material in Figure 4 can be very well approximated with an exponential function of the form $A(s) = Ce^{-s/\lambda}$. Analogously, the same parameterization can also be used for the charge (see Figure 5). The fitting parameters found (using an implementation in *Mathematica*) for the charge z as a function of penetration depth s in the material are $C = 81$ and $\lambda = 5.95$. We can now overestimate the spectrum of fragments as $82/z(s)$ fragments each of charge $z(s)$. In reality there will normally be only one heavy fragment and many much smaller. Integrating the total energy lost by these fragments over 29 cm by inserting the fitted formula for *z(s)* and multiplying with the number of these fragments, the total energy loss of the ion over this distance is only 4.1 A GeV. According to the Bethe-Bloch formula the energy loss per unit path length dE/dx for the initial $^{208}Pb^{82+}$ ion is 0.69 A GeV/cm, or 0.56 A GeV/cm if one takes the crude approximation that the energy loss stays constant above 100 GeV/nucleon. So, even if we overestimate the energy loss and suppose that an ion does not fragment, it will lose less than 20.1 A GeV over 30 cm through ionization, which is still less than 1% of its total energy. The extra contribution from pair production is even smaller.

This shows that direct electromagnetic interactions are only a minor contribution to the total energy deposition from a primary particle (which is totally dominated by the hadronic shower and the electromagnetic shower resulting from it), but very localized due to the large number of soft electrons created. So, when considering lost ions entering an LHC magnet, it is reasonable to expect that the energy deposition will differ from protons when averaged over a very small volume just around the track of the impinging ion. However, when averaging over larger volumes and, thus, also over parts of the magnet further away from the track of the ion, the hadronic shower will be the dominating factor. As a result, the overall shower profile for heavy ions and protons will be very similar.

Because of the very steep angle of the beam losses, which in the case of the generic simulated loss is 0.25 mrad, the impinging particle will traverse a large distance inside the beam screen before it actually reaches the superconducting coils. Thus one might expect that the shower profiles will differ in a small volume around the track of the ion/proton in the beam screen but not on a macroscopic scale and not in the superconductor. The result of a FLUKA simulation shown in Figure 6 and Figure 7 demonstrates that this is indeed the case. In Figure 6, the energy deposition was scored in the beam screen in a mesh with transverse dimensions $0.1 \times 0.1\ \text{mm}^2$ and 1 cm longitudinally. In Figure 7, the energy was instead

averaged over the whole 1 mm thickness of the beam screen and, even on this small scale the ionization loss by the heavy ions is much smaller than the hadronic shower.

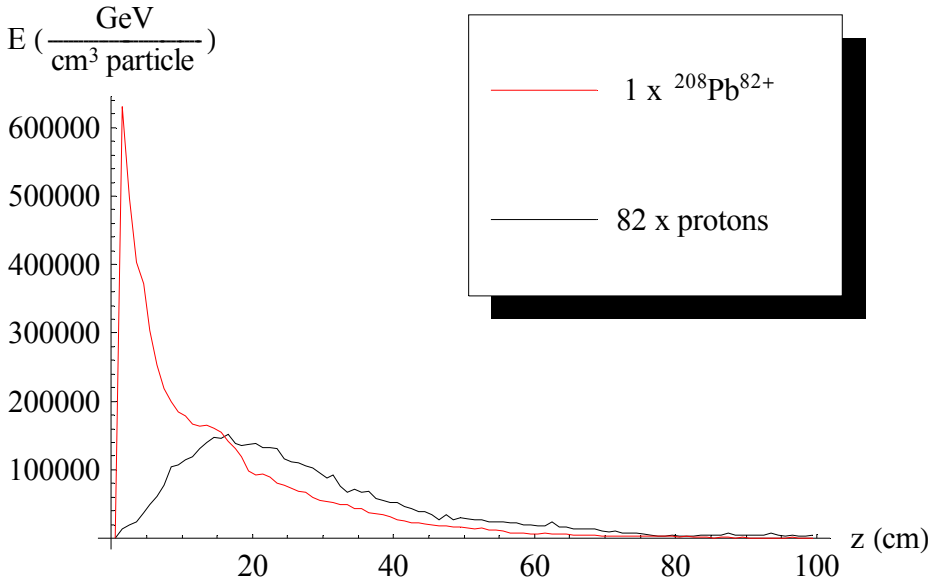

Figure 6. The energy deposition for Pb ions and protons at LHC energy in the innermost 0.1 mm of the beam screen.

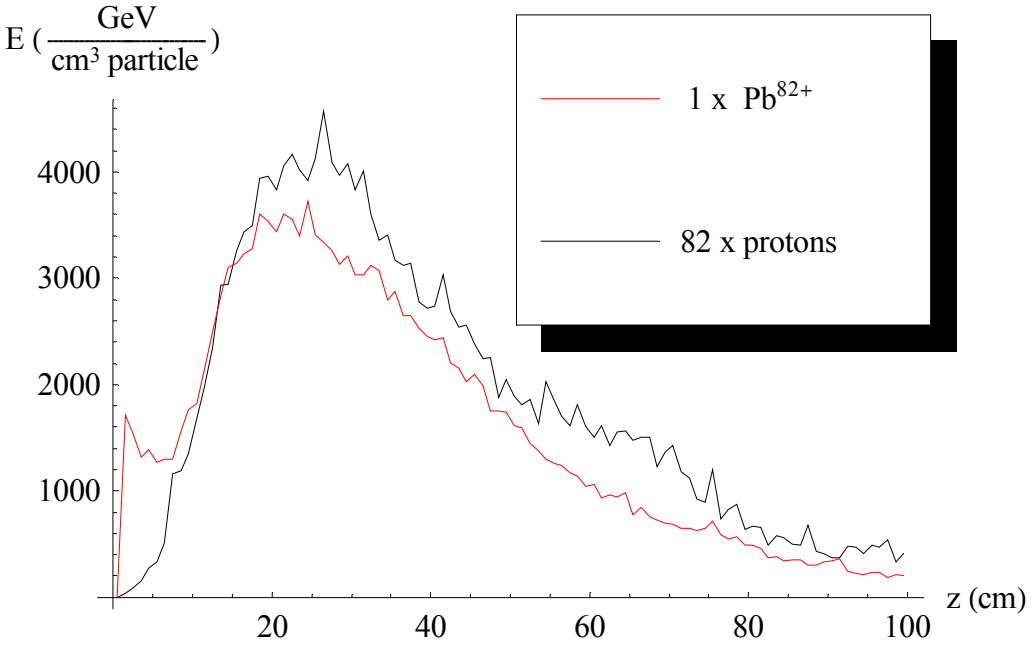

Figure 7. The energy deposition for the two species in the beam screen averaged over 1 mm^2 transversely.

On a larger scale and farther away from the impinging particle, for instance in the coils, the shower profile should be similar, since most of the energy will be lost in the charge-independent hadronic shower. The larger scales are also much more relevant for machine protection, since the size of the minimum propagating zone[1] for a quench in a LHC superconducting magnet is on the scale of 1 cm [19]. On smaller scales quenches will die out

[1] The minimum propagating zone is the largest volume of a superconductor which can go into a normal conducting state without causing a quench.

by themselves and can be reabsorbed by the material. On the 1 cm scale only the hadronic shower is visible, as is evident from Figure 2.

Moreover, practically all the particles entering the BLMs originate from the hadronic shower. Thus it can be expected that the ratio between the power deposited in the coil on a 1 cm scale and the energy deposited in the BLMs outside the cryostat should be similar. This means that the same thresholds can be used for dumping the beam, in agreement with the result of the FLUKA simulations in the previous section.

3. Monitoring losses from collimation

The LHC collimation system has been designed for proton beams of high intensity and is based on a two-stage collimation concept, with short primary collimators intercepting particles, and long secondary collimators downstream where the halo particles, scattered off the primaries, deposit their energy in hadronic showers [14]. In spite of having 100 times less beam power, problems arise for ion collimation because the mechanisms of particle-collimator interaction are different and more complicated: hadronic fragmentation and electromagnetic dissociation upon impact on primary collimators result in the production of particles with small angle divergence and different charge-to-mass ratio that can fail to be intercepted by secondary collimators and can produce significant heat load in the superconducting magnets with the attendant risk of quenches. At present, the cleaning efficiency falls short by about a factor of 2 for the nominal ^{208}Pb ion beam at collision energy and therefore a suitable system of monitoring loss spots has to be put in place.

Simulation studies for ion collimation have been carried out using the ICOSIM program, which combines particle tracking capabilities with treatment of heavy ion specific interactions. A detailed description of the program can be found elsewhere [15]. We assumed the latest LHC optics description (V6.500) and aperture model and simulated ion losses over 250 turns of the machine for 50,000 initial particles, a beam lifetime of 12 minutes and two different energy scenarios: at injection (energy per nucleon $E/A = 177.4$ GeV) and collision ('nominal case', $E/A = 2.76$ TeV).

All Phase I [16] primary (TCPs) and secondary (TCSs) collimators in IR3 and IR7 have been included in the study, together with all the tertiary collimators protecting the interaction regions. Standard aperture settings were assumed at both energy levels, as listed in table 1.

	n_1	n_2	n_3
Injection IR3	8	9.3	10
Injection IR7	6	7	10
Collision IR3	15	18	10
Collision IR7	6	7	10

Table 1 Aperture settings of primary, secondary and tertiary collimators (n_1, n_2, n_3 respectively) in terms of the beam σ.

For the betatron collimation study case, a 4D shell beam distribution is initially generated with an emittance of 36 times the nominal value, corresponding to particles scraping the jaws of the primary collimators (positioned at 6σ) in the horizontal and vertical phase space projections. Particles are then tracked through the machine lattice using linear transfer matrices in *x, x', y, y', δp/p*, taking into account linear dispersion in the bending magnets, chromaticity effects in the quadrupoles and sextupole effects in thin element kick approximation. Beam acceleration is not included in the study, on the grounds that the RF synchrotron period is considerably longer (about a factor of 500 at collision) than the time needed for a full machine turn. Upon impact on the collimators, multiple scattering and

ionisation energy loss are calculated analytically, whereas the probability for nuclear fragmentation is derived from look-up cross section tables. If the ion effective path inside a collimator is larger than 10 times the interaction length, the particle is assumed to be stopped. If on the other hand the particle is lost on the aperture, its exact hit position is found by interpolation and recorded. An artificial increase in the transverse coordinates is carried out every 100 revolutions in order to simulate the beam diffusion process. Both this 'beam blow-up' factor and the parameter giving the thickness of the initial shell beam density control the impact parameter distribution of the ions on the primary collimators. The dependence of the collimation inefficiency (defined as ratio of the number of particles lost on the aperture over the number stopped in the collimators at a particular turn of the machine) on the average value of the impact parameter was the object of a detailed study aimed at calibrating the input parameters of the code and finding a reasonable setup for the loss studies.

Figure 8 shows the linear correlation between the effective path length travelled by the lead ions inside the collimators and the average impact parameter upon the first machine turn. The collimation inefficiency calculated after the first turn ($\eta(1)$) presents a somewhat expected behaviour, falling off at high impact parameters (the longer the distance travelled the higher the probability that the particles are stopped and absorbed in the collimators). However, after 250 turns, this dependence proves to be more complicated, as the efficiency improves also for very small values of the impact parameter. This has been shown to be due to a multi-turn effect, whereby particles that are scattered off at their first impact with a collimator, eventually hit at a later revolution with a much bigger impact parameter (factor 10-100) and are consequently effectively stopped in the collimator. The turning point between the two regimes, at around <b>=0.7-0.8 μm, corresponds to the case where the effective path length in the TCPs is comparable to the average nuclear interaction length (~2.5cm for lead ions). For the studies presented in this note, the 'skin depth' (i.e. density shell thickness) parameter in the code has been set to yield <b>=0.66 μm, or L_{eff}=2 cm.

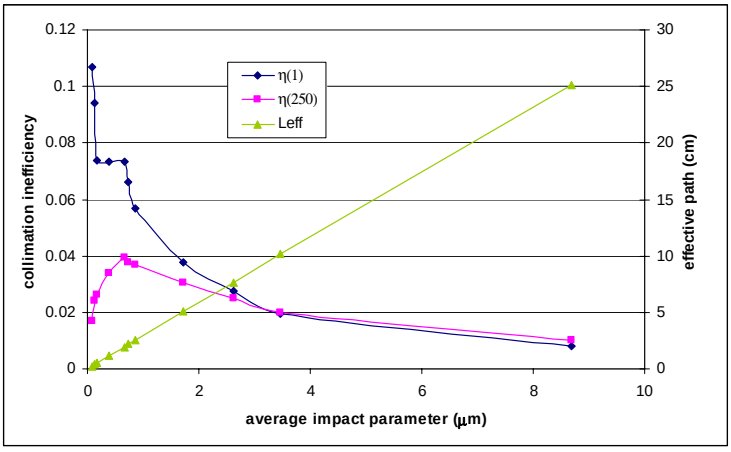

Figure 8: Variation of the effective path length (green) and collimation inefficiency after one (blue line) and 250 (magenta) turns of the machine as a function of the average impact parameter on primary collimators.

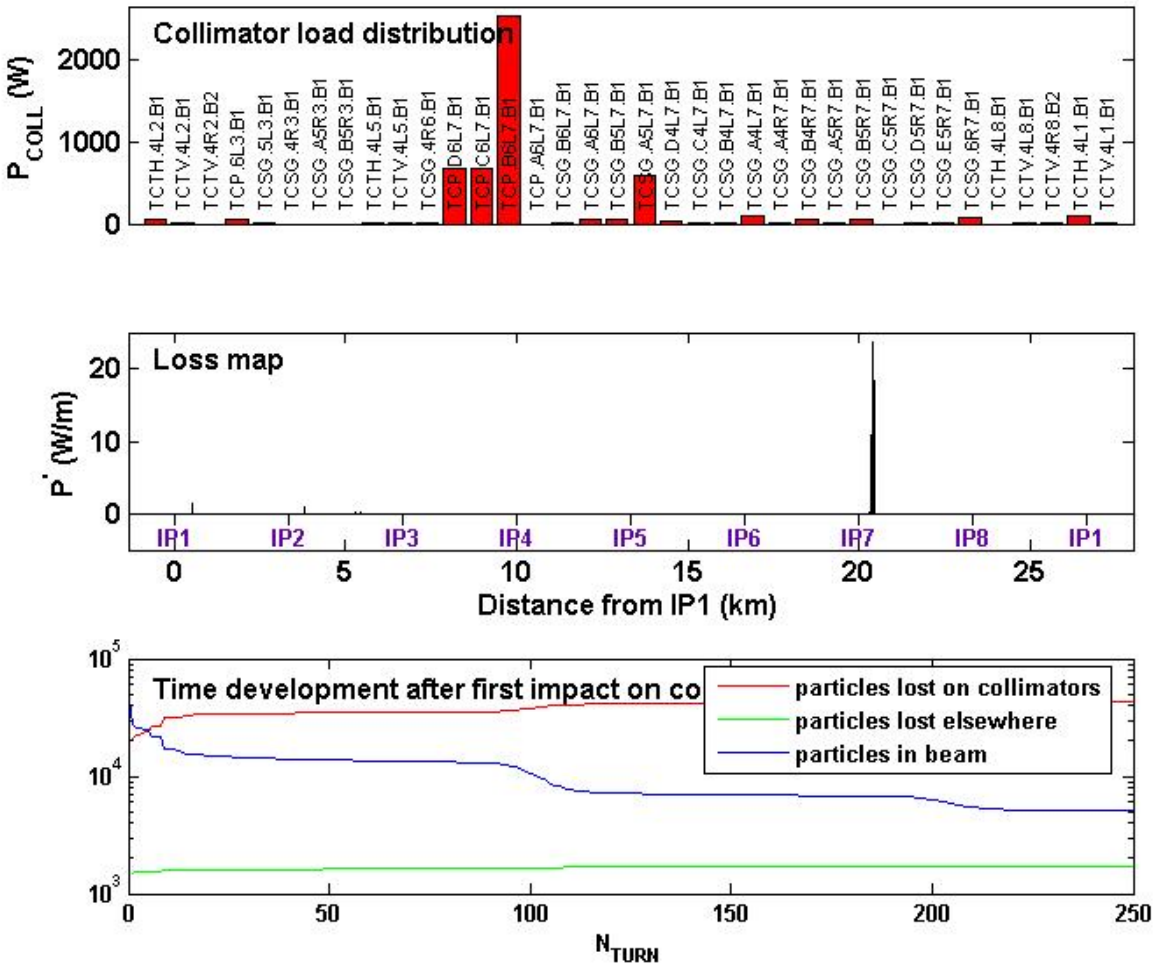

Figure 9 Simulation results for beam 1 at top energy.

Figure 9 shows the results of simulations for beam1 at nominal collision energy: the top plot shows how the heat load is distributed almost only on the primary collimators, with a very little fraction borne by the secondaries. Losses on the machine aperture are concentrated in the IR7 dispersion suppressor (centre plot). The evolution in time of the losses is shown in the bottom plot over a span of 250 turns of the machine: the collimation inefficiency calculated at the end of the run is around 4%. Figure 9 shows the corresponding spectrum of ion losses in the IR7 dispersion suppressor region against the machine lattice shown at the bottom: contributions from different ion species are represented by different colours in the histogram. At this energy value all the loss peaks tend to be very narrow and localised, with a clear separation between different ions' contributions. At more than one location the maximum heat deposition is well above the average quench limit along the machine (8.5 W/m)[17]

Beam2 presents a quantitatively and qualitatively very similar loss spectrum, except that in this case losses are not exclusively confined to the dispersion suppressor, but are also present with a couple of peaks (Pb^{206} and Hg^{201}) further down in the arc.

At injection energy, on the other hand, the power load deposited is in general a factor 20-50 smaller than at collision, and the loss spectrum is also qualitatively different, with very broad areas of losses and not so easily distinguishable contributions from the various ion

species (see Fig.10), the smearing of the loss distribution being due to the much larger geometric emittance of the beam at lower energies.

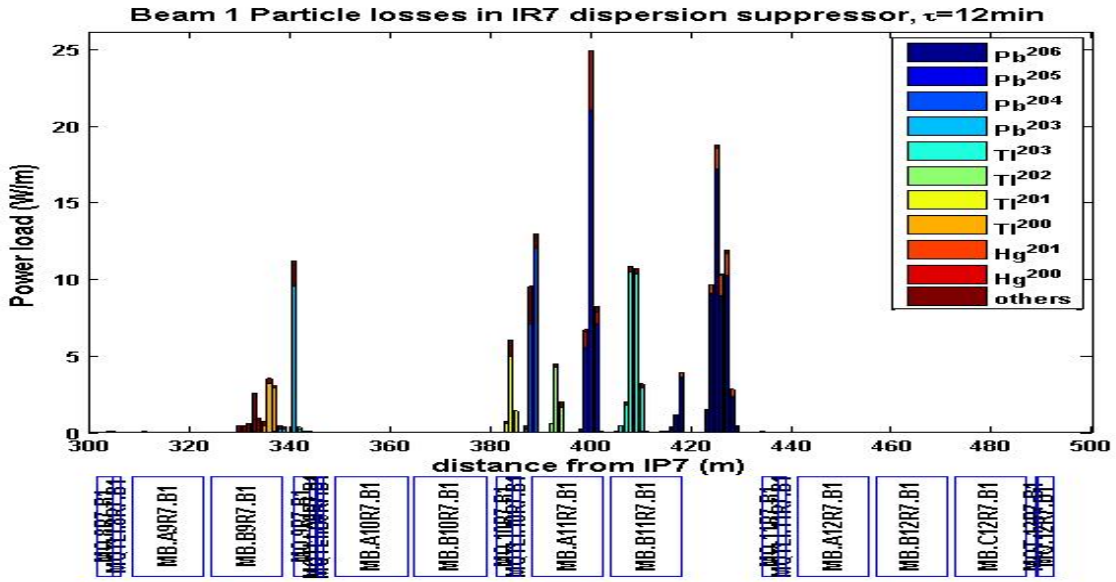

Figure 10 Loss spectrum in the IR7 dispersion suppressor for beam1 at collision energy.

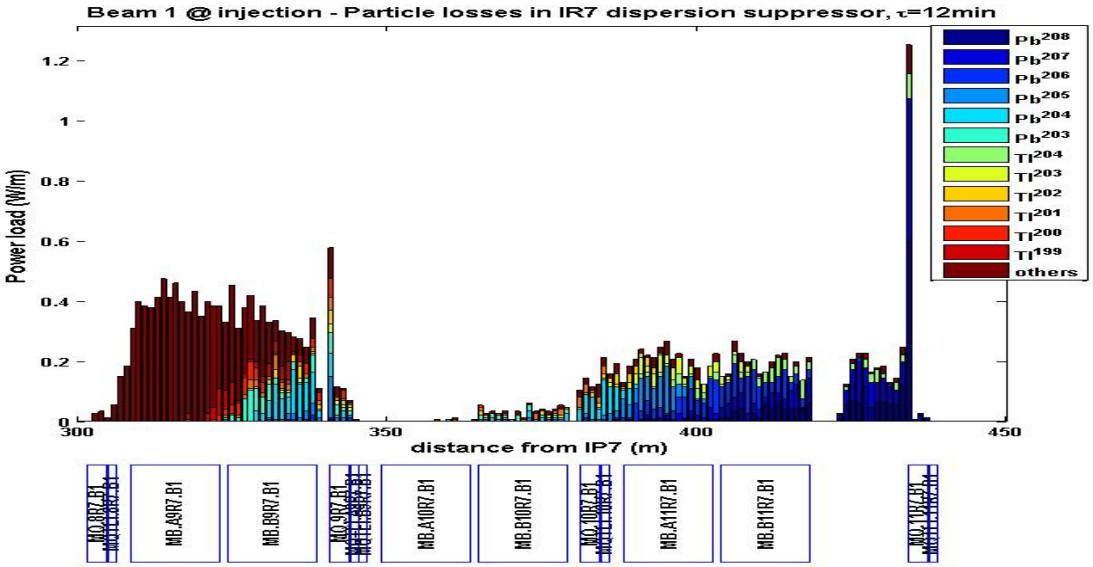

Figure 11 Loss spectrum in the IR7 dispersion suppressor for beam1 at injection energy.

A slightly different code setup is used to study momentum collimation. A Gaussian beam with nominal RMS emittance is initially generated, with a $\delta p/p$ following a parabolic probability distribution between a minimum and a maximum values a and b, with b equal to the momentum offset corresponding to the primary collimator gap height (at the collimator location), and with a derived from b after subtracting four times the momentum offset corresponding to the sigma of the beam. Tracking and fragmentation physics are modelled in the same way as per the betatron collimation studies. Figure 11 shows the geometric distribution of the ion hits onto the primary collimator and a histogram of their momentum offsets at the first machine turn.

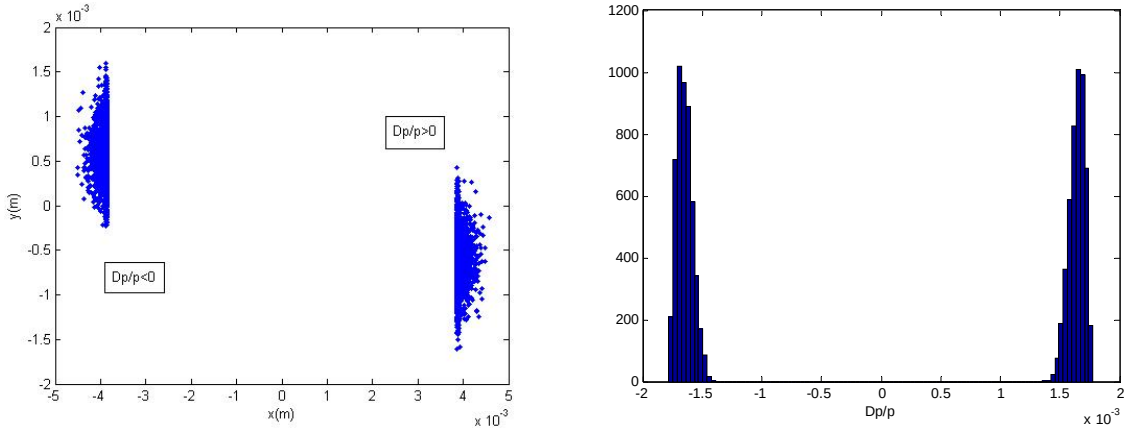

Figure 12 Particle hit distribution on the primary collimator at first passage (left) and histogram of their momentum offsets (right).

The momentum collimation efficiency in IR3 is comparable to what was found for betatron collimation in IR7 (quantitatively), with η=4.6% after 250 revolutions. Qualitatively, however, there is a difference since most of the particles are stopped in the IR3 collimators after just a few turns (see Fig.12 at the bottom).

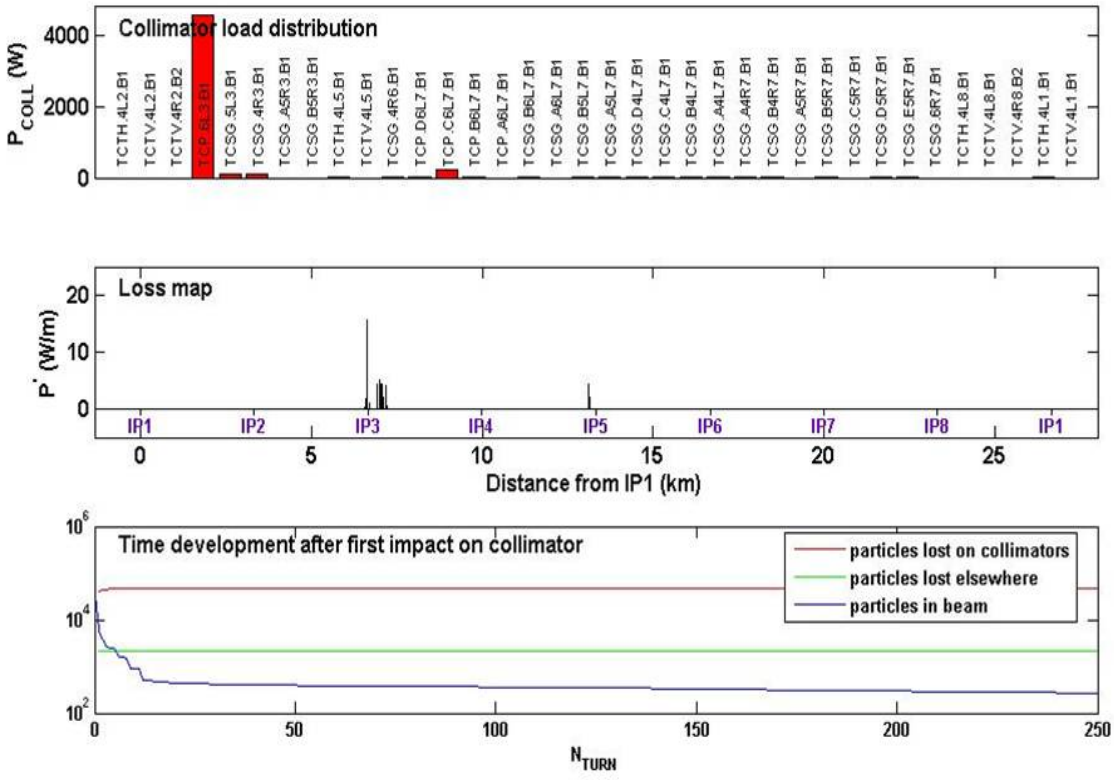

Figure 13 Momentum collimation statistics for beam1 at collision energy.

For the settings used in the simulations, the average impact parameter onto the primary collimator is ~37 μm, nearly a factor of 50 larger than the average value for betatron cleaning; as a consequence ions are already more effectively absorbed on the collimator jaws in the first few passages. Figure 13 shows the results of a study of the dependence of the collimation inefficiency on the average impact parameter after 2 and 250 turns of the machine. Even at the smaller values of the impact parameter the mean effective path length travelled in the primary

collimator is well above the average nuclear interaction length for lead ions (λ~2.5cm) so the probability for the particle to be absorbed at first impact is relatively high. Also, intuitively, the larger the impact parameter the more efficient is the cleaning process (and the difference between the two curves η(2) and η(250) shrinks to zero).

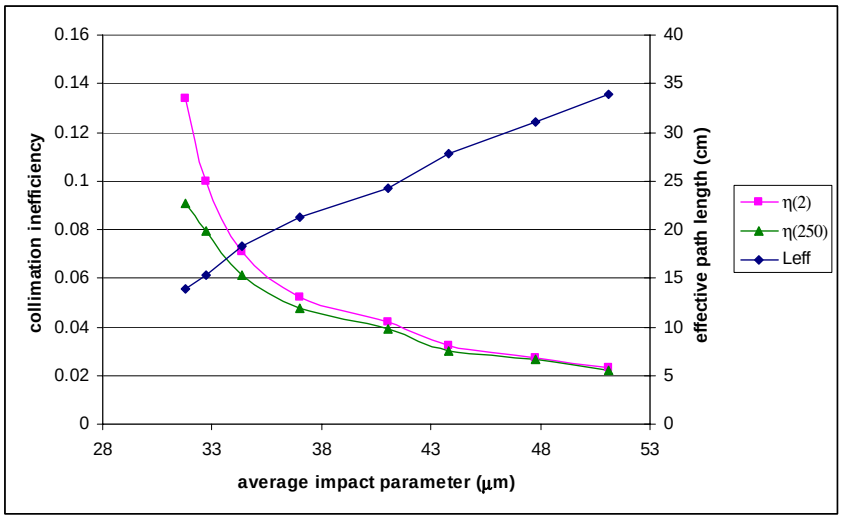

Figure 14: Momentum collimation inefficiency as a function of the average impact parameter.

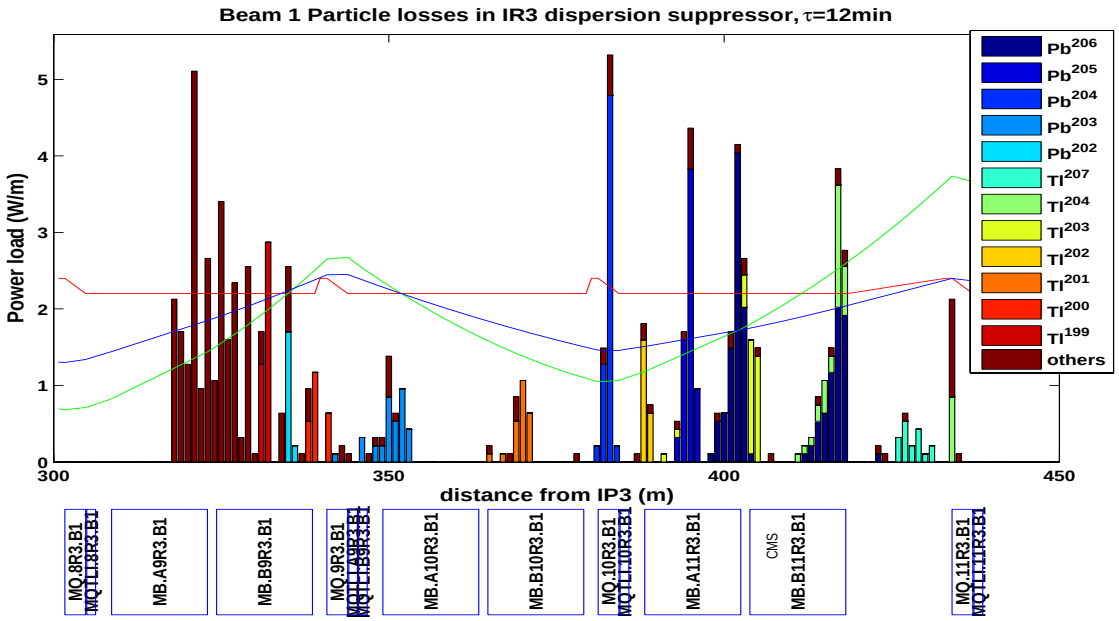

Figure 15: Beam loss spectrum in IR3 dispersion suppressor for beam1 at collision energy (in blue and green are the horizontal dispersion and beta function respectively, while showin in red is the machine aperture, not to scale).

Figure 15 shows the beam loss spectrum on the machine aperture of the IR3 dispersion suppressor for beam1 at collision energy. The heat load deposited is considerably lower than for IR7 (and below the nominal average quench limit) and a higher concentration of peaks typically occurs in zones of increasing dispersion. Outside the dispersion suppressor, some

losses have been recorded in the warm region of the machine just upstream of the IP3 interaction point and in the arc downstream. The first ones are caused by ion species with a very different rigidity than lead ions and do not require any particular protection system to be put in place. The second ones, on the other hand, are concentrated in cell 13 of the arc, at approximately a π phase advance from the primary collimator, and are mainly caused by Pb^{207} and Tl^{204}, particularly ions with an initially negative momentum offset. Simulations for beam 2 have shown similar results.

The dependence of the loss pattern on possible orbit movements has been estimated for the time being with a study of the effect of changes in the aperture on the peaks positioning and heat load distribution. The aperture data used also has a safety margin of 1 mm, meaning that the real aperture could be up to 1 mm wider. Several scenarios were investigated, either increasing (or decreasing) flatly the aperture everywhere along the machine or just alternately opening and closing some sections, following the periodic focusing scheme. The conclusions finally reached were that an increase (decrease) of the aperture by a few mm tends to produce a shift downstream (upstream) of the loss peaks of up to 10m, but without crossing the boundaries of the dispersion suppressor region.

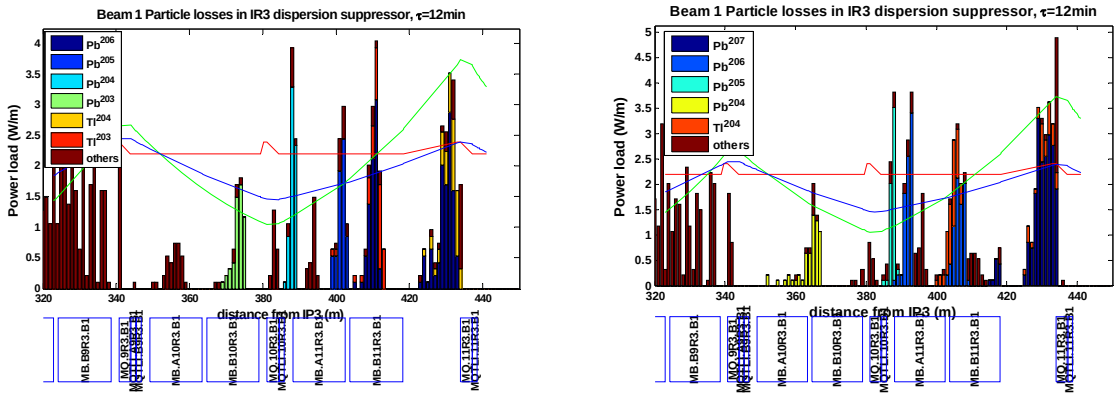

Figure 16 : Beam loss spectra in the IR3 dispersion suppressor region for a +4mm (left) and -4mm (right) aperture. Shifts in the peaks locations are noticeable by comparison with Figure 15.

Given this uncertainty and the fact that the loss peaks tend to be very narrow and localised, a machine protection programme based on a very tight coverage of all loss areas with BLMs has been proposed. FLUKA simulations have shown that the full-width at half-maximum of the energy deposition signal in the BLM gas is 2.5 m for a pencil beam loss (see Figure 2 at the bottom), and that the maximum of the signal occurs approximately 1.5m downstream from the impact point.

Therefore a 2.5 m spacing between chambers has been assumed for both beams to ensure full detection of losses, relaxed to 3.75-4 m spacing in less critical areas. On top of the BLMs already foreseen for proton operation, which are mounted on all quadrupoles in the arcs and dispersion suppressors [9], the installation of extra chambers for specifically monitoring ion losses has therefore been requested. The constraints imposed by the limited number of instrumentation patches available, 8 channels per patch, has made it necessary at certain locations to connect two BLMs on the same readout channel, even though this will make it hard to distinguish between two superimposed non-dangerous losses reported by two different BLMs and one dangerous localised loss monitored by a single BLM. This complicates the setting of dump thresholds. Furthermore it will make the distinction of signals for spectroscopy studies more difficult. A complete list of positions of the BLMs proposed for IR7 and IR3 is given in Appendix A.

4. Monitoring losses from interactions in collision

When the Pb^{82+} ion beams collide at an IP, a number of electromagnetic processes peculiar to ion operation take place [8]. Some of these cause the ions to change their charge to mass ratio, in some cases so much so that the affected ions constitute secondary beams that leave the design trajectory and are lost somewhere in the machine. These secondary beams can cause a high localized energy deposition that may quench a magnet and it is therefore important to monitor the spots where they are lost.

The most dangerous process is Bound Free Pair Production (BFPP), where one of the colliding ions captures an extra electron, resulting in a secondary beam emerging in both directions from the IP. Explicitly written, the reaction is:

$$^{208}Pb^{82+} + {}^{208}Pb^{82+} \xrightarrow{\gamma} {}^{208}Pb^{82+} + {}^{208}Pb^{81+} + e^{+}$$

The corresponding change of magnetic rigidity of the $^{208}Pb^{81+}$ beam is 0.012, which is twice the limit of the machine acceptance of 6×10^{-3} [10], meaning that these ions will be lost in the machine. The danger of a quench induced by this BFPP beam has already been investigated elsewhere (see [11] and references therein). There the impact of the BFPP beam on an LHC main dipole was simulated in a FLUKA simulation. It was concluded that the energy deposited in the superconducting coils by the BFPP beam is not likely to quench a main LHC dipole if it hits in the middle of the magnet. However, if the beam instead hits near the end it could be more dangerous since the cooling of the conductors in this region is less effective because of the coil design. Experiments at RHIC have shown that orbit errors easily can move the BFPP spot several metres [12], meaning that in the LHC there will be a danger that the BFPP spot might move from a harmless position to a dangerous one. Therefore it is of highest importance to monitor this loss in the LHC.

To determine the impact locations of the BFPP beam on both sides of every IP where ions may collide (IP1, IP2, IP5), ions with the appropriate change of magnetic rigidity were tracked in the LHC lattice in the Madtomma environment, as in [13]. Tracking was performed both in the nominal optics and in the early ion scheme optics for beam one and two. The wrongly charged BFPP beam follows the (locally generated) dispersion function and losses may occur when this function becomes large enough. The orbits obtained in the tracking were compared with detailed aperture data in order to determine the loss locations.

Small orbit errors were also taken into account. Realistic angular offsets at the IP are estimated to be less than 10 μrad. When the initial conditions of the tracking at the IP were varied, the impact position moved by approximately 10 cm. An initial horizontal offset of 0.1 mm was also considered. This offset moves the loss position by about 2 m at IP2 but only 27 cm at IP1 and IP5. The interval of the impact positions obtained for each IP and scheme is shown in Table 2. The typical longitudinal spread of the losses is of the order of 2 m at IP2 and 6 m at IP1 and 5 for a 3 σ beam. The second loss interval in the table is from the secondary impact position described in detail later.

Expected impact position s (m)	IP1	IP2	IP5
Nominal beam 1	429-434, 539.5-541.5	378.5-381.5, 474.5-477.5	429-433.5, 535-536
Nominal beam 2	416.5-420, 539	379-381.5	417.5-421, 532
Early beam 1	414	378.5-381.5	415
Early beam 2	412	375.4	413

Table 2. Expected impact locations of the central particle for beam 1 and 2 for each IP in the early ($\beta^* = 1.0$ m) and nominal ($\beta^* = 0.5$ m) scheme.

Simulations were also performed with the aperture increased by 1 mm, and the observed effect was that the loss location could move several metres. A summary of the influence of these conditions is shown in Table 3.

Movement of primary BFPP impact location (m)	IP1	IP2	IP5
±10 μrad angle at the IP	±0.36	±0.09	±0.35
±0.1 mm offset at the IP	±0.27	±2	±0.27
1mm extended beam pipe	3.2	1.0	3.2

Table 3. The influence of orbit errors at the IP and an extended beam pipe on the primary BFPP loss location for the various IPs.

In Figure 17, Figure 18 and Figure 19 the 5σ envelope of the BFPP beam coming out of IP1, IP2, and IP5 is shown together with the aperture. From these figures, it is clear that at IP1 and IP5 a fraction of the beam escapes the primary location where the central particle first hits the beam pipe and is instead lost further downstream at a secondary impact point. At IP2 however all particles even at 5 σ are lost at the first impact location. Figure 20 shows a 3D picture of the BFPP beam coming out of IP2 together with the nominal beam.

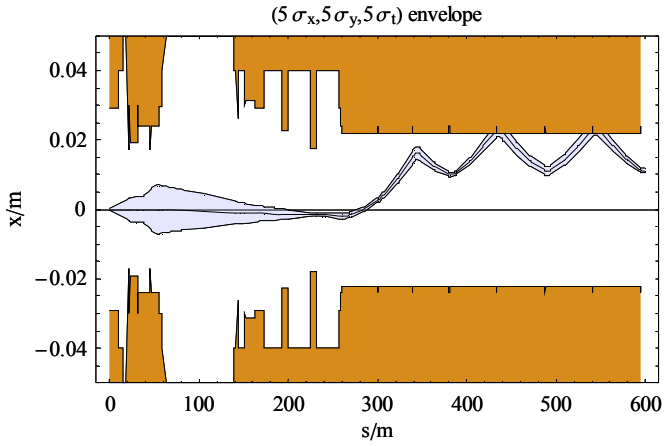

Figure 17. The 5 σ beam envelope in the x-plane of the BFPP beam coming out of IP1 shown together with the aperture.

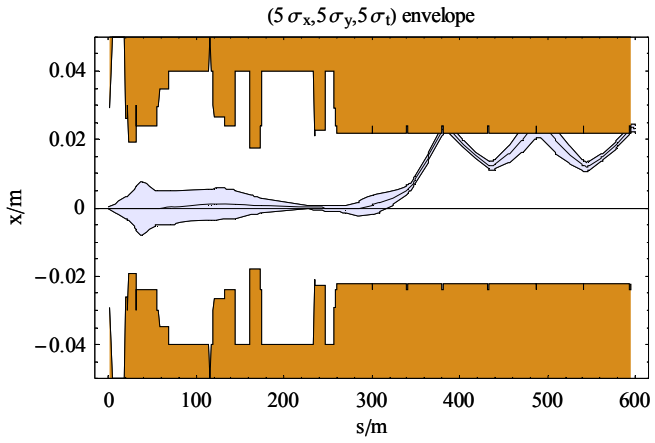

Figure 18. The 5 σ beam envelope in the x-plane of the BFPP beam coming out of IP2 shown together with the aperture.

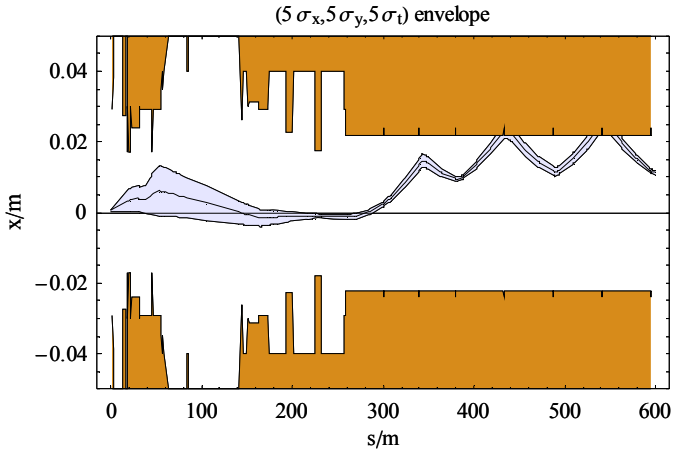

Figure 19. The 5 σ beam envelope in the x-plane of the BFPP beam coming out of IP5 shown together with the aperture.

Orbit errors also influence whether the particles are lost at the primary or secondary loss location. Further tracking shows that without errors, particles are lost at IP1 and IP5 at the second peak of the trajectory already within the 1σ envelope, while at IP2 the beam envelope has to be extended to 6 σ before particles go further downstream. This means that practically the whole beam will be lost at the first location. In **Error! Reference source not found.** a summary is shown of the fraction of the beam that is lost at the primary and secondary impact location.

% of BFPP beam lost at:	IP1	IP2	IP5
primary spot, no orbit errors	99.7	100	100
Secondary spot, no orbit errors	0.3	0	0
primary spot, with orbit errors	85	47	94
Secondary spot, with orbit errors	15	53	6

Table 4. The relative fractions of the BFPP beam lost at the various impact locations with and without orbit errors at the IP.

It is worth noting that the fact that parts of the BFPP beam escapes to locations further downstream is in fact beneficial from a machine protection point of view, since the heat load will be spread out in other elements. If only half of the BFPP beam is lost at the primary position it gives an extra margin of a factor two to the quench limit.

The locations of the BLMs needed have been determined by tracking studies. It is clear from the sensitivity analysis in Table 3 that the impact point can move several metres due to uncertainties in the orbit. Measurements done at RHIC of the BFPP process confirm that this is the case [12]. If the BFPP beam hits near the end of a magnet instead of in the middle, it can be crucial, since heat load levels from the BFPP losses are expected to be around the quench limit of the main dipoles [11].

Also for monitoring BFPP it was decided to have a very tight BLM coverage. However the number of needed BLMs is much smaller for this loss type than for collimation losses and there is also an intrinsic scientific interest in the BFPP process—it has only been measured once before on a high energy collider [12] and more detailed measurements could help to confirm theoretical results on the BFPP cross sections. Therefore it was decided to make an even tighter coverage of 1.5 m, which also makes it possible to make more detailed estimates of the precise loss locations and the actual heat load on the superconductors. It was also decided to hold to the principle of having only one BLM per channel, due to the complications with superimposed signals described in the previous section. Extra BLMs were proposed in all loss locations, both primary and secondary, that were not already covered by the monitors foreseen for protons. The proposed extra BLMs for BFPP, together with the

expected impact positions and the code names for the elements where the beam is expected to be lost are shown in Table 5 in Appendix A.

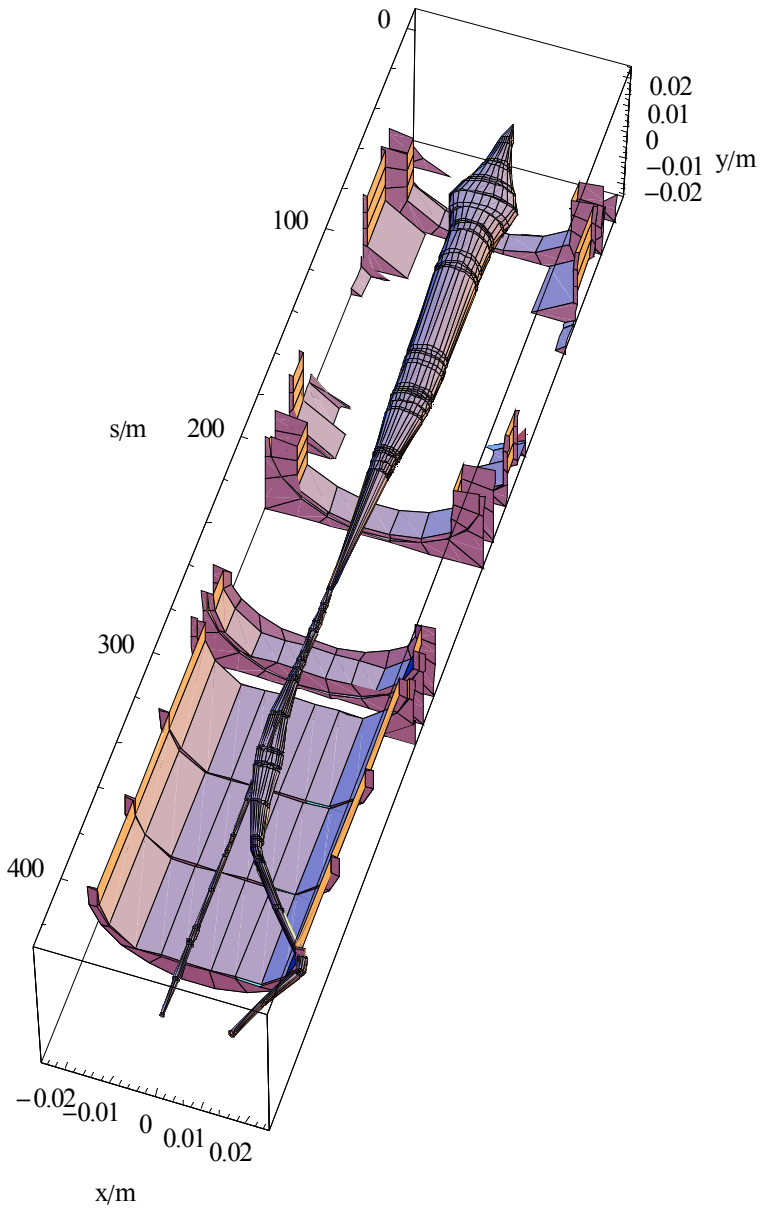

Figure 20. The 5 sigma beam envelope of the BFPP beam and the main beam coming out from IP2 shown together with the aperture (which is cut away outside the range of the plot axes).

BFPP is the most important and dangerous electromagnetic process creating beam losses, but other mechanisms also exist and should be examined. One such process that takes place at the IP is electromagnetic dissociation (EMD). Here an ion loses one or two neutrons through the field of another one. In the first case, the change in magnetic rigidity is smaller: $\delta = -0.005$. Thus the affected ions remain within the momentum acceptance of the ring so that they will be absorbed in the momentum-cleaning insertion with a rate determined

by the contribution of this process, with $\sigma_{1n}^{EMD} \approx 215$ b, to the luminosity lifetime, 1/(a few hours) at most [10,18]. Figure 21 shows the orbit of the central EMD particle going out from IP2.

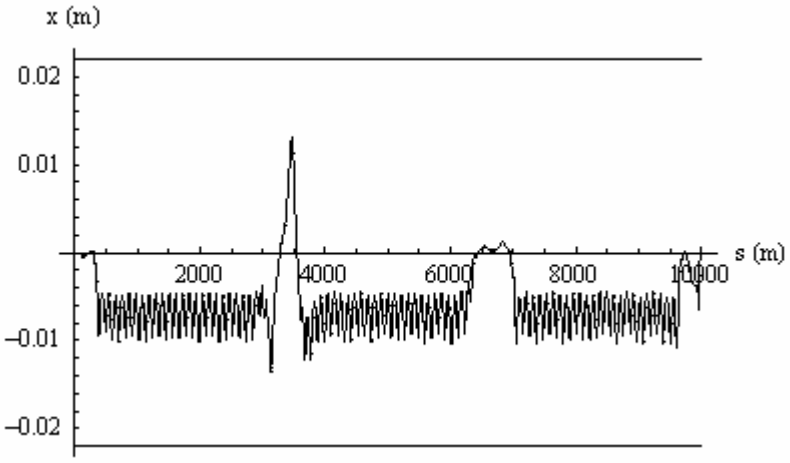

Figure 21. The 1 neutron EMD beam coming out of IP2, without taking account of the momentum collimation around IR3.

In the second case, where two neutrons are emitted, the corresponding change in magnetic rigidity is larger: $\delta = -0.0096$. Loss spots are apparently formed only in the warm parts of IR3, where the dispersion generated since IP2 reaches sufficiently large values, and the cross section is also somewhat smaller: $\sigma_{2n}^{EMD} \approx 0.3\sigma_{1n}^{EMD}$ [18] so the rates can be expected to be correspondingly lower. If the optics or aperture is not ideal, these losses are likely to take place at QF quadrupoles in the arcs where there is already BLM coverage.

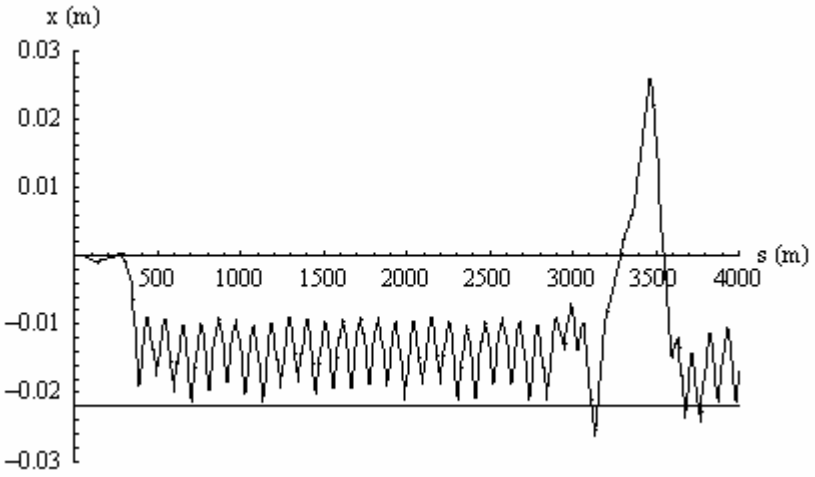

Figure 22. The trajectory of the central particle in the two neutron EMD beam coming out of IP2. The particle is lost at 3100 m downstream from the IP.

Since the losses caused by the one neutron process have too small a momentum deviation to form a localized spot and the two neutron process leads to losses in warm sections (or possibly in the arcs), it was concluded that no extra BLMs need to be installed to monitor losses from EMD at the IP.

5. Conclusions

The energy loss of $^{208}Pb^{82+}$ ions and protons inside a material is different because of the high ionization cross section of the ions. However, when lost particles hit the inside of an LHC magnet, the difference is only visible in the beam screen. This implies that the ratio between heat deposition in the coils and BLM signal is approximately the same for Pb^{82+} ions and protons and that the same thresholds for dumping the beam can be used.

Extra BLMs are needed for ion operation to monitor losses from BFPP and from collimation inefficiency. The expected loss locations have been determined by appropriate tracking methods and an installation of BLMs has been specified. EMD does not appear to pose a risk of quenching in new locations and it appears that no extra BLMs are needed for this process.

The optimal locations for BLMs depend on the loss locations which, in turn, depend on the physical aperture available to the beam. It follows that they may need to be revised in the event of any changes to the optics or the aperture (e.g., installation of detectors close to the beam) in the relevant regions.

6. Acknowledgements

We thank B. Dehning, A. Ferrari, J-B. Jeanneret, M. Magistris, L. Ponce and G.I. Smirnov for profitable discussions and information.

7. References

[1] E.B. Holzer et al, CERN-AB-2006-009, 2005

[2] A. Fasso et al, CERN-2005-10

[3] A. Fasso et al, arXiv:hep-ph/0306267, 2003

[4] S. Eidelman et al, “Review of Particle Physics”, Physics Letters B, 592:1+, 2004.

[5] J. Lindhard, A. Sørensen, “Relativistic theory of stopping for heavy ions,” Phys. Rev. **A53**, pp. 2443-2456 (1996).

[6] G.I. Smirnov, private communication, 2006

[7] H.H. Braun et al, "Hadronic and electromagnetic fragmentation of ultrarelativistic heavy ions at LHC", Elsevier preprint (2004).

[8] The LHC Design Report, Vol. I, CERN-2004-003 Chapter 21 and references therein.

[9] E.B. Holzer et al, "Beam Loss Monitoring System for the LHC ", CERN-AB-2006-009 (2005).

[10] J. M. Jowett. Ions in the LHC ring. Proceedings of the LHC Performance Workshop, Chamonix XII, 2003.

[11] R. Bruce, S.S. Gilardoni, J.M. Jowett, CERN LHC Project Note 379 (2006)

[12] J.M Jowett, R. Bruce, S.S. Gilardoni, A. Drees, W. Fischer, S. Tepikian, S.R. Klein, “Measurement of ion beam losses due to bound-free pair production in RHIC, Proceedings of EPAC 2006, MOPLS010, 553 (2006).

[13] J.M. Jowett, H.H. Braun, M.I. Gresham, E. Mahner, A.N. Nicholson, E. Shaposhnikova, I.A. Pshenichnov, “Limits to the Performance of the LHC with Ion Beams”, Proceedings of EPAC 2004, MOPLT020 (2004).

[14] T.Trenkler, J-B.Jeanneret, CERN-SL/95-03

[15] H.H. Braun, R. Aßmann, A. Ferrari, J.B. Jeanneret, J.M. Jowett, I.A. Pshenichnov, "Collimation of Heavy Ion Beams in LHC", Proceedings of EPAC2004, MOPLT010 (2004).

[16] The LHC Design Report, Vol. I, CERN-2004-003 Paragraph 18.3,
R. Aßmann, Proposal to the AB LHC Technical Committee (LTC) on June 25th 2003.

[17] J. B. Jeanneret, D. Leroy, L. Oberli and T. Trenkler, LHC Project Report 44 (1996).

[18] I. A. Pshenichnov, J. P. Bondorf, I. N. Mishustin, A. Ventura, and S. Masetti, Mutual heavy ion dissociation in peripheral collisions at ultrarelativistic energies, Phys, Rev, C64 (2001) 024903-1.

[19] F. Sonnemann. Resistive transition and protection of LHC superconducting cables and magnets. PhD thesis, RWTH Aachen, 2001.

[20] G Schatz et al, J. Phys. G: Nucl. Part. Phys. **20** 1267-1281, 1994

[21] L.K. Ding et al, The astrophysical Journal **474** 490-495, 1997

Appendix A:

Table 5. The proposed locations of new BLMs for monitoring BFPP losses, together with the MADX names of the elements where they will be mounted

BEAM	IP	SLOT	s (m, from IP)	Inside or Outside	MadX Name
1	1	LBBRA.11R1	411.8 413.9 416.0 418.1	Outside	MB.B11R1.B1
		LEHR.11R1	420.2 431.4 433.5 435.6	Outside	Drift_50
		LBBRD.13R1	537.9 540	Outside	MB.C13R1.B1
1	2	LBBLF.10R2	369.0 371.1 373.2 375.3 377.4 379.5	Inside	MB.B10R2.B1
		LBALB.12R2	480.5 482.6	Inside	MB.C12R2.B1
1	5	LBBRA.11R5	411.8 413.9 416.0 418.1	Outside	MB.B11R5.B1
		LEGR.11R5	420.2 431.4 433.5 435.6	Outside	Drift_63
		LBBRC.13R5	536.0 538.1	Outside	MB.C13R5.B1
2	1	LBALA.11L1	409.7 411.8 413.9 416.0 418.1	Outside	MB.B11L1.B2
		LEFR.11L1	420.2 422.3 424.4	Outside	Drift_46
		LBALA.13L1	538.9 541	Outside	MB.C13L1.B2
2	2	LBARE.10L2	366.9 369.0 371.1 373.2 375.3 377.4 379.5	Inside	MB.B10L2.B2
		LBBRA.12L2	480.5 482.6	Inside	MB.C12L2.B2
2	5	LBALA.11L5	411.8 413.9 416.0 418.1	Outside	MB.B11L5.B2
		LEFL.11L5	420.2 422.3 424.4	Outside	Drift_59
		LBALA.13L5	538.0 540.1	Outside	MB.C13L5

Table 6 Proposed locations of BLMs for monitoring losses due to collimation inefficiency, together with the slot reference and the MAD-X names of the elements where they will be mounted.

BEAM	IP	SLOT	s(m) from IP7	Transv pos	MAD-X name	cold mass type
1	7	BJBAP.A9R7		Outside	MB.A9R7.B1	MBA.9R7
			317			
			320			

			322.5			
			325			
			327.5			
			330			
			332.5			
			335			
1	7	BJBAP.B9R7				
			338.2			
			346.65	Outside	MQ.9R.B1	MQ.9R7
1	7	BJBAP.A10R7		Outside	MQ.10R7.B1	MQ.10R7
			376.2			
			378.7			
			386.4			
1	7	BJBAP.A11R7		Outside	MB.A11R7.B1	MBA.11R7
			391			
			393.5			
			396			
			398.5			
			401.2			
			404.6			
			406.1			
			408.5			
			411.5			
			413.5			
			415.7			
			417.7			
1	7	BJBAP.B11R7		Outside	MQ.11R7.B1	MQ.11R7
			439.2			
2	7	BJBAP.A9L7		Inside	MB.A9L7.B2	MBB.9L7
			320			
			322.5			
			325			
			327.5			
			330			
			332.5			
			335			
			337.5			
			340			
			342.5			
2	7	BJBAP.A11L7		Inside	MB.B11L7.B2	MBA.11L7
			388.5			
			391			
			393.5			
			396			
			398.5			
			401			
			403.5			
			406			
			408.5			
			411			

			413.5			
			416			
			418.5			
2	7	BJBAP.B11L7		Inside	MQ.11L7.B2	MQ.11L7
			433			
2	7	BYPLM.A13L7		Inside	MQ.13L7.B2	MQ.13L7
			538.5			
			541			
2	7	BYPLM.A19L7		Inside	MQ.19L7.B2	MQ.19L7
			854			
			856.5			
			859			
			861.5			
BEAM	**IP**	**SLOT**	**s(m) from IP3**	**Transv pos**	**MAD-X name**	**cold mass type**
1	3	BJBAP.B9R3		Inside	MB.B9R3.B1	MBB.9R3
			315.5			
			318			
			320.5			
			323			
			325.5			
			328			
			330.5			
			333			
			335.5			
			338			
1	3	BJBAP.A9R3		Inside	MQ.9R3.B1	MQ.9R3
			350			
			353.75			
			357.5			
			361.25			
1	3	BJBAP.A10R3		Inside	MQ.10R3.B1	MQ.10R3
			365			
			368.75			
			372.5			
			376.25			
1	3	BJBAP.A11R3		Inside	MB.A11R3.B1	MBA.11R3
			388			
			390.5			
			393			
			395.5			
			398			
			400.5			
			403			
			405.5			
			408			

			410.5			
			413			
			415.5			
			418			
1	3	BYPLM.A12R3		Inside	MQ.12R3.B1	MQ.12R3
			512			
			515.75			
			519.5			
			523.25			
1	3	BYPLM.A13R3		Inside	MQ.13R3.B1	MQ.13R3
			527			
			530.75			
			534.5			
			538.25			
2	3	BJBAP.B9L3		Outside	MB.B9L3.B2	MBA.9L3
			315.5			
			318			
			320.5			
			323			
			325.5			
			328			
			330.5			
			333			
			335.5			
			338			
2	3	BJBAP.A9L3		Outside	MQ.9L3.B2	MQ.9L3
			350			
			353.75			
			357.5			
			361.25			
2	3	BJBAP.A10L3		Outside	MQ.10L3.B2	MQ.10L3
			365			
			368.75			
			372.5			
			376.25			
2	3	BJBAP.A11L3		Outside	MB.B11L3.B2	MBA.11L3
			388			
			390.5			
			393			
			395.5			
			398			
			400.5			
			403			
			405.5			
			408			
			410.5			

			413			
			415.5			
			418			
2	3	BYPLM.A12L3		Outside	MQ.12L3.B2	MQ.12L3
			512			
			515.75			
			519.5			
			523.25			
2	3	BYPLM.A13L3		Outside	MQ.13L3.B2	MQ.13L3
			527			
			530.75			
			534.5			
			538.25			